

## **A PHYSICS-BASED LANDMINE DISCRIMINATION APPROACH WITH COMPRESSIVE SENSING**

**Pengyu Wang<sup>\*</sup>, Qian Song, and Zhimin Zhou**

College of Electronic Science and Engineering, National University of Defense Technology, Changsha 410073, China

**Abstract**—Compressive Sensing (CS) is a recently developed technique, which can reconstruct the sparse signal with an overwhelming probability, even though the signal is sampled at highly sub-Nyquist rate. Based on the observation that the electromagnetic scattering structure (ESS) of a metal landmine is composed of two scattering centers, whose geometrical parameters are tightly related to its physical dimensions, a new physics-based landmine discrimination approach is proposed in this paper. Firstly, the approach uses the Multi-Measurement Iterative Pixel Discrimination method to reconstruct the landmine's ESS in noisy environments. Secondly, the geometrical parameters of the landmine's ESS are extracted from the sparse image. Thirdly, landmine discrimination is conducted according to the measured geometrical features and apriori knowledge. Finally, the field experimental results demonstrate the effectiveness of the proposed approach.

### **1. INTRODUCTION**

Compressive Sensing (CS) [1] is a recently proposed technique for data acquisition and processing. It allows the sparse signal to be reconstructed just with a random measurement, which is usually much smaller than the demands of Nyquist sampling theorem. As the number of targets is much smaller than that of the resolution cells in the detection area, CS has been widely and successfully applied to radar imaging [2–8]. But applying the CS to target discrimination and recognition is really worthy of further investigation. The key is how to use CS to extract target's electromagnetic scattering structure (ESS) and combine it with discrimination methods effectively.

---

*Received 27 August 2012, Accepted 26 November 2012, Scheduled 10 December 2012*

\* Corresponding author: Pengyu Wang (kedawangpengyu@yahoo.com.cn).

This paper is on the basis of the Forward Looking Ground Penetrating Virtual Aperture Radar (FLGPVAR) system which is designed to detect the flush buried metal landmines. As the system adopts the techniques of Split Transmitting Virtual Aperture (STVA) and Stepped Frequency Continuous Wave (SFCW) [9], it has the capability of high 2-dimension resolution. And moreover, it can obtain the data of any frequency point from arbitrary receive channel, which makes the preparation for CS application as well. Since landmine detection belongs to the typical problem of static dim target detection in the complex environment, there are few effective solutions until nowadays [10]. According to Ref. [11], the electromagnetic scattering model of landmine can be approximately to be an isotropic symmetrical cylinder, which is close to a combination of two discrete scattering centers. The corresponding geometrical feature parameters correlate highly with both the system imaging model and the physical structure of landmine, and furthermore, they have definite physical senses and consistent properties. These conclusions inspire us that it is possible to use CS to extract landmine from the sparse image of minefield and implement discrimination via landmine's apriori knowledge.

In the real environments, the noise with unknown statistical distribution always contaminates the radar echoes of landmine. Noise violates the sparse precondition of CS reconstruction and makes the extraction of landmine's ESS inaccurate or even unrealizable. The Gradient Projection (GP) algorithm [12], which is grounded on the regularization programming, provides a possibility for robustly extracting the ESS of landmine, but the performance of GP is heavily enslaved to the regularization parameter  $\lambda$ . The selection of  $\lambda$  is a fundamental problem within a regularization framework, and it has been resolved by several existing approaches, such as Stein's unbiased risk estimator, generalized cross validation (GCV), graphical tools and so on [13]. When the noise is unknown, the GCV algorithm performs much more proper than the others on  $\lambda$  estimation. However, under the low signal-to-noise ratio (SNR) conditions, the GCV has difficulty in guaranteeing  $\lambda$  converge at the global optimum, which becomes an obstacle for accurate CS reconstruction. For solving the problem, the Multi-Measurement Iterative Pixel Discrimination (MM-IPD) approach is presented.

The reminder of this paper is organized as follows. Section 2 describes the basic theory of CS and then presents the MM-IPD approach. The electromagnetic analysis of landmine, as well as the imaging model introduction of the FLGPVAR system, is presented in Section 3. Sparse feature extraction and landmine discrimination are discussed in Section 4. Section 5 shows the experimental results

processed by the proposed approach. Conclusions and discussions are drawn in Section 6.

## 2. COMPRESSIVE SENSING AND MM-IPD APPROACH

The CS theory points that a sparse and/or compressible signal  $x$  of length  $N$  can be acquired via a linear measurement as [13]

$$y = \Phi x + w = \Phi\Psi\alpha + w = \Theta\alpha + w \quad (1)$$

where  $\Phi$  represents the measure matrix,  $w$  stands for the additive white Gaussian noise with variance  $\sigma^2$ ,  $y$  and  $\alpha$  represent measured data and sparse coefficient vector respectively. If  $x$  is sparse in the known domain  $\Psi$  and the matrix  $\Theta = \Phi\Psi$  satisfies the Restricted Isometry Property (RIP) [14, 15], then  $\alpha$  can be recovered from Eq. (2).

$$\hat{\alpha} = \arg \min \|\alpha\|_1 \quad \text{s.t.} \quad \|\Theta\alpha - y\|_2 < \varepsilon \quad (2)$$

where  $\varepsilon = \sqrt{2\log N}\sigma$  is the residual energy threshold of the reconstructed error [4], and it is obvious that the solution of  $\alpha$  depends heavily on  $\varepsilon$ . If the  $\sigma$  is unknown, the choice of  $\varepsilon$  will become not straightforward and hard to be estimated. Alternatively, one can recover  $\alpha$  from the following equation which belongs to the regularization programming method.

$$\hat{\alpha} = \arg \min (\|\Theta\alpha - y\|_2^2 + \lambda\|\alpha\|_1) \quad (3)$$

where  $\lambda$  is the regularization parameter which balances the measurement residual errors and the signal sparsity. Although Eq. (3) is different from Eq. (2), they are equivalent to each other for solving the same problem [16]. And moreover, Ref. [13] also points out that both  $\lambda$  and  $\varepsilon$  are data dependent, but the relationship between them is unknown. We can effectively solve  $\alpha$  without knowing the noise by solving Eq. (3), but the precondition is that the optimal  $\lambda$  has to be estimated beforehand.

When noise is unknown, the GCV algorithm behaves suitable for estimating  $\lambda$  [13]. It estimates  $\lambda$  by minimizing the predictive error. In most cases, the GCV estimation curve exhibits unimodal. But the numerical approximations involved by the GCV are prone to make the curve oscillate when the SNR is low. This oscillation will induce estimation errors and make  $\lambda$  hard to converge at the optimum especially around small values. As a result, it is difficult to reconstruct the noisy signal accurately if only using one single measurement and reconstruction. However, the MM-IPD approach introduced afterward gives a feasible and efficient solution for robust reconstruction of noisy signal in low SNR conditions. It effectively eliminates the affect of

$\lambda$  estimation error on CS reconstruction and enhances the Signal-to-Clutter Ratio (SCR) of the reconstructed image. The composition of the MM-IPD is shown as follows:

- a) CS processing with multiple measurements
  - multiple random extractions of the measured data;
  - estimation of parameter  $\lambda$  with the GCV;
  - reconstruction with Eq. (3);
- b) Iteratively clustering the reconstructed pixel series with the Time Series Clustering (TSC) algorithm [17].

As Eq. (3) is a nonlinear optimum programming problem, its non-analytic solution makes the Probability Density Function (PDF) of either target or clutter hard to be expressed analytically. However, the Monte Carlo (MC) simulation method gives an effective way for resolving the problem. Fig. 1(a) is the recovery curve of target and clutter when SNR changes from  $-15$  dB to  $0$  dB with the interval  $5$  dB. For each SNR,  $1000$  CS reconstructions are actualized. Fig. 1(b) is the nonzero amplitude histogram of target and clutter with SNR being  $-15$  dB. In terms of Ref. [18], the PDF of clutter is a mixture model composed of a Dirac function at zero and a generalized Pareto (GP) PDF, which is in accordance with the clutter histogram and the dash line in Fig. 1(b), whereas the target histogram seems to fit to the Gaussian distribution approximatively.

According to Fig. 1, it is not hard to find that accurate reconstruction with one single measurement seems unreachable when the SNR is below  $-15$  dB, but target has the statistical separability from clutter on amplitude. For target, the proportion of nonzero value will gradually converge at the reconstruction probability along with the increase of MC number, which is the premise of applying the MM-IPD.

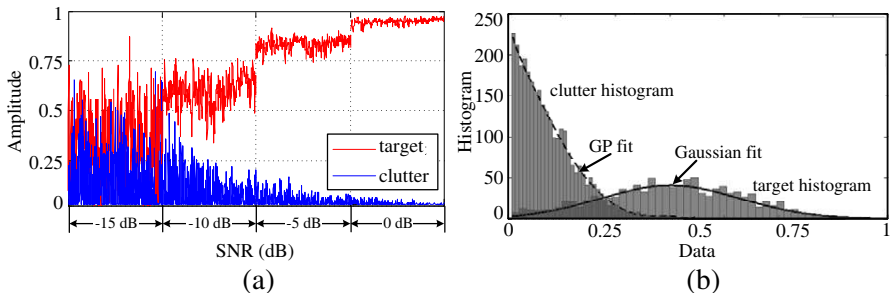


**Figure 1.** CS reconstruction based on MC simulations under different SNR conditions, (a) recovery values, (b) histogram with SNR equaling to  $-15$  dB.

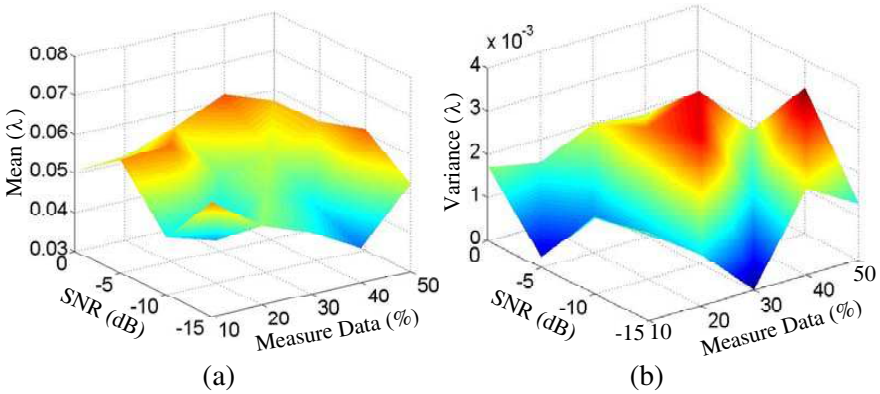


**Figure 2.** Statistical values of  $\lambda$  versus SNR and measured data (%), (a) mean, (b) variance.

It is concluded that target usually has a consistent nonzero center of the recovered amplitude series, but clutter inclines to a near-zero value.

Using similar simulation settings to Fig. 1, Fig. 2 shows the curves of mean and variance values of  $\lambda$ , which is estimated by GCV with different measure matrices (corresponding to different data percents) under various SNR conditions. In addition, for each pair of SNR and measure matrix 100 MC simulations are actualized. The results in Fig. 2(a) indicates that when the SNR is below 0 dB, the estimated values of  $\lambda$  oscillate in a small region (i.e.,  $([10^{-2}, 10^{-1}])$ ). Though the estimated variance changes in a merely small scope, the estimated error lays heavy effect on CS reconstruction, which has been demonstrated by the foregoing results in Fig. 1(a).

In order to measure the quality of the constructed image, we define two new variables: sparsity difference of image  $E_{SDI}$  and energy difference of image  $E_{EDI}$

$$\begin{cases} E_{SDI} = \left| \|\hat{\alpha}_{TSC}^l\|_S - \|\hat{\alpha}_{TSC}^{l-1}\|_S \right| \\ E_{EDI} = \left\| \hat{\alpha}_{TSC}^l - \hat{\alpha}_{TSC}^{l-1} \right\|_2 \end{cases} \quad (4)$$

where  $\hat{\alpha}_{TSC}^l$  is the sparse vector processed by the  $l$ th CS reconstruction and TSC clustering. The norm “ $\|\cdot\|_S$ ” in  $E_{SDI}$  is defined as the number of targets whose amplitudes exceeding a small positive threshold.

From the 2-dimension feature curves in Fig. 3, it can be implied that  $E_{SDI}$ , as well as  $E_{EDI}$ , has a similar variation tendency that their values are inversely proportional to SNR and iteration number. Now in terms of the above discussions, the procedure of the MM-IPD approach

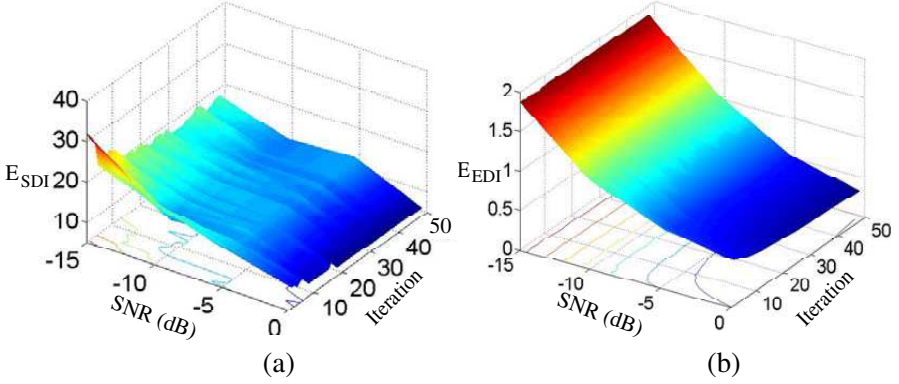


**Figure 3.** Feature curves of the reconstructed image in different SNRs and iteration numbers, (a)  $E_{SDI}$ , (b)  $E_{EDI}$ .

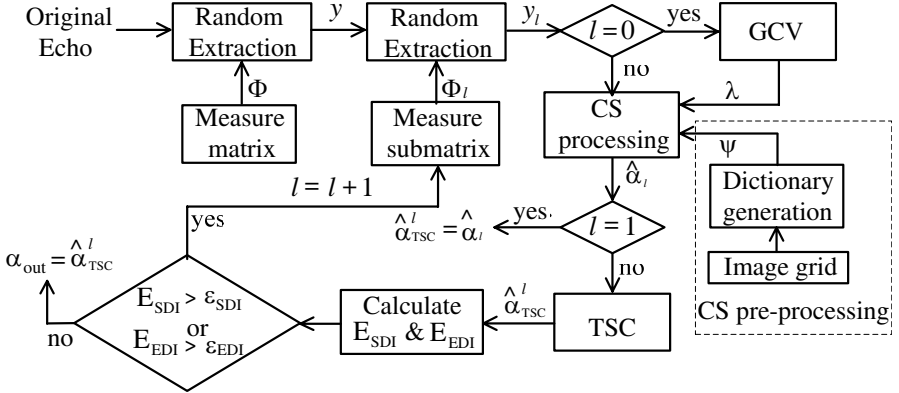


**Figure 4.** Processing flow of the MM-IPD approach.

is introduced step-by-step, and the corresponding processing flow is shown in Fig. 4 as well.

- 1) The CS imaging space is meshed, and the dictionary  $\Psi$  is generated;
- 2) The original measure matrix  $\Phi$  is used to obtain the measured data  $y$ ;
- 3) The measure submatrix  $\Phi_l$ , which is the subset of  $\Phi$ , is generated, and the measure subset  $y_l$  is randomly extracted from  $y$ ;
- 4) If  $l = 0$ , the parameter  $\lambda$  is estimated by the GCV algorithm with  $\Phi_l$ ,  $y_l$ , and  $\Psi$ , otherwise jump to step 5;
- 5) Equation (3) is solved with  $\Phi_l$ ,  $\Psi$ ,  $\lambda$ , and  $y_l$ ;

- 6) If  $l = 1$ ,  $\hat{\alpha}_{TSC}^l = \hat{\alpha}_l$ ; otherwise,  $\hat{\alpha}_{TSC}^l = TSC([\hat{\alpha}_1, \dots, \hat{\alpha}_l])$ , and  $E_{SDI}$  and  $E_{EDI}$  are calculated by Eq. (4);
- 7) If either  $E_{SDI} > \varepsilon_{SDI}$  or  $E_{EDI} > \varepsilon_{EDI}$  (where  $\varepsilon_{SDI}$  and  $\varepsilon_{EDI}$  are the preset decision thresholds, i.e.,  $\varepsilon_{SDI} = 0.05 * \|\hat{\alpha}_{TSC}^l\|_S$ ,  $\varepsilon_{EDI} = 0.05 * \|\hat{\alpha}_{TSC}^l\|_2$ ),  $l = l + 1$  and return to step 3, otherwise, the iteration is terminated.

To demonstrate the effectiveness of the MM-IPD approach, five randomly positioned point-like targets are simulated. Except for special declaration, all the measure matrices used in this paper are the random Bonulli matrix which is constructed by randomly selecting some rows of the identity matrix [4]. Meanwhile, the measure submatrix  $\Phi_l$  ( $l \geq 0$ ) is a subset of  $\Phi$ , and it is generalized by randomly selecting some rows of  $\Phi$ . Under the same simulation conditions with Fig. 2(b), Fig. 5 shows the processing results of the MM-IPD approach, and Fig. 6 is the corresponding iterative curves of targets

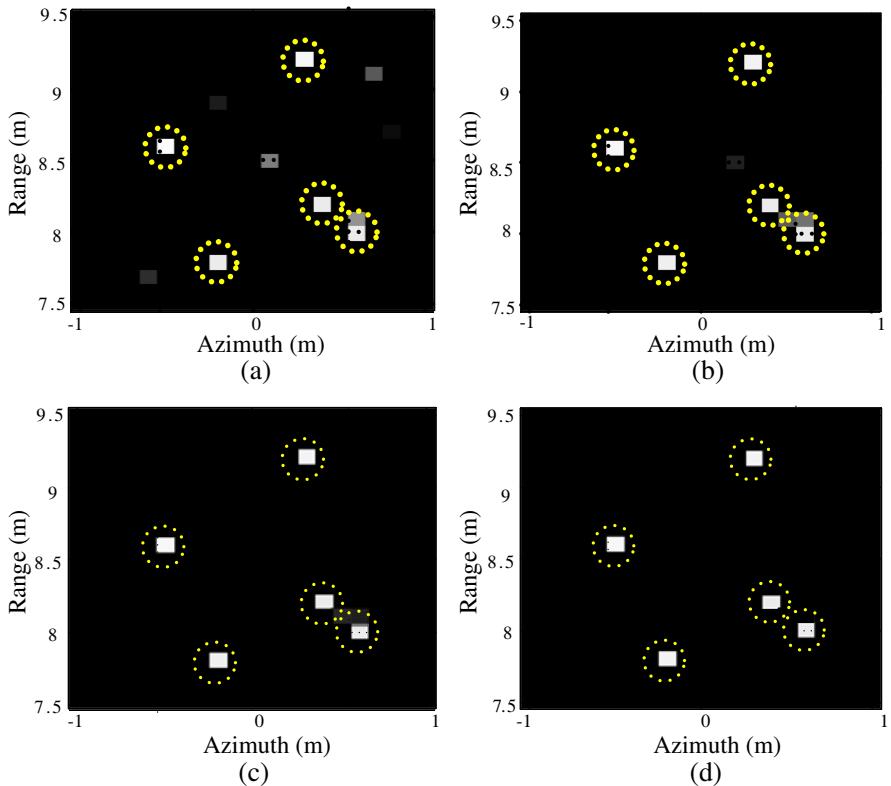


**Figure 5.** Simulation results of MM-IPD with total iteration numbers: (a) 1, (b) 5, (c) 10, and (d) 15.

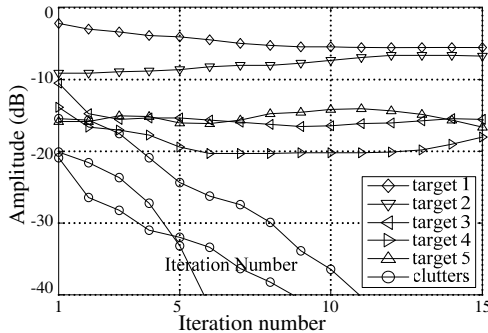


**Figure 6.** MM-IPD iteration curve of targets and clusters.

and clusters. From the results in either Fig. 5 or Fig. 6, it can be concluded that when the iteration number reaches 15, all the targets are accurately reconstructed except for amplitude losses, while the clutters are effectively suppressed.

### 3. ELECTROMAGNETIC CHARACTERISTIC OF LANDMINE AND IMAGING MODEL OF THE FLGPVAR SYSTEM

#### 3.1. Electromagnetic Scattering Characteristics of Landmine

Nowadays, electromagnetic modeling has become a useful tool for analyzing target scattering characteristic, and especially it has played an important role in landmine detection for the Ground Penetrating Radar (GPR) system [19]. Based on the simulated results of the improved Physical Optics (PO) method and the BoomSAR experimental results [20], the Army Research Laboratory (ARL) investigates the 1-dimension features of metal landmine. Both the simulated and experimental results draw the same conclusion that the metal landmine has the double-hump feature. Meanwhile, the Stanford Research Institute (SRI) yields a similar conclusion, but it is based upon the Method of Moment (MoM) and the FLGPR system [21]. Additionally, aiming at the flush buried metal landmine, Ref. [11] proposes the calculation method of the 2-dimension electromagnetism and builds the scattering model with the PO method. With some approximations, it also presents the analytical expression of the radar echoes. The simulated results illustrate that the flush buried metal landmine has a similar feature of double-hump, whose ESS correlates with the physical structure and can be quantitatively analyzed. Due to the ultra-wide bandwidth and long emission wavelength of the

FLGPVAR system, the discontinuous plane of electromagnetic wave usually exhibits one single point-like reflector in the received echoes. That means the double-hump of the metal landmine can approximate two discrete scattering centers which are separated in the down-range direction. In the field experiments, this situation exists in both echoes and images. According to [11], the landmine can closely approximate a cylinder which is shown in Fig. 7, where  $h$  and  $r$  denote the height and radius, respectively,  $d$  represents the buried depth which is the distance between landmine's upper surface and the ground.

Equation (5) shows the 1-dimension received echo  $S_r(k)$  of landmine in the wavenumber domain

$$S_r(k) = P(k)H_s(k, \theta_i, \varepsilon_r)\{A_1 \exp[-j2k(R_0 - r \sin \theta_i)] + A_2 \exp[-j2k(R_0 + r \sin \theta_i)]\} \quad (5)$$

where  $A_1$  and  $A_2$  are the amplitudes of the double-hump, and  $P(k)$  is the transmit signal,  $k$  the wavenumber,  $\theta_i$  the radar incident angle,  $\varepsilon_r$  the soil relative permittivity,  $R_0$  the distance between radar and the ground projection of landmine's upper surface center,  $H_s$  the influencing factor of refraction and dispersion on the received echo, which is written as

$$H_s(k, \theta_i, \varepsilon_r) = T(\theta_i, \varepsilon_r) \exp\left(-j2kd\sqrt{\varepsilon_r - \sin^2 \theta_i}\right) \quad (6)$$

where  $T(\theta_i, \varepsilon_r)$  is the transmission coefficient of the electromagnetic wave penetrating soil and air twice. Here, we define a new variable  $M_{GD}$  which represents the ground distance of landmine's double-hump. By solving (5) and (6) simultaneously, we can come to the conclusions:  $M_{GD}$  is approximately equal to  $2r$ , which appears completely irrelevant to  $\theta_i$ . In despite of using the high-frequency approximation, the PO modeling method quantitatively shows two characteristics of landmine: invariant azimuth scattering and double-

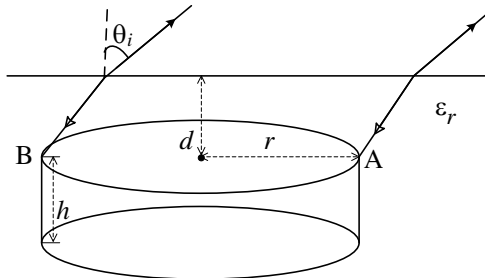


**Figure 7.** Approximate electromagnetic model of landmine.

hump. To all appearances, they both determined by the physical structure are suitable for landmine discrimination and recognition.

### 3.2. Imaging Model of the FLGPVAR System

Compared with the conventional monostatic system, the FLGPVAR system can use less antennae and STVA technique to obtain a comparable azimuth resolution if provided with the same aperture length. On the ground of Ref. [22], the range side-lobe of the FLGPVAR system parallels the tangent of the ISO metry Doppler (ISO-Doppler) curve, and it is irrelevant to the position of the transmit antenna. For landmine, the side-lobes of its double-hump (defined as point  $A$  and point  $B$  in Fig. 8) are consistent with each other, and the line connecting  $A$  and  $B$  parallel the range axis. In other words  $A$ ,  $B$  and  $O$  (virtual aperture center) ought to be in the same line. In addition, we define a new angle variable  $\varphi$  named azimuth virtual angle in this paper. It represents the angle between connecting line from scattering center to virtual aperture center  $O$  and radial direction. As regards landmine, the azimuth virtual angles of  $A$  and  $B$  should approximately equal to each other (i.e.,  $\varphi_A \approx \varphi_B$ ), and the values are only correlated with the relative positions between the virtual aperture center and the landmine.

## 4. FEATURE EXTRACTION AND LANDMINE DISCRIMINATION

From the previous discussions, we can arrive at the conclusion that both the double-hump distance and the azimuth visual angle belong to the prior geometric features of landmine. But owing to the mismatch between CS image grid and landmine model, each of the double-hump might have the possibility of falling on several grids. Consequently, the reconstructed image usually needs the clustering processing. Furthermore, in order to enhance the discriminating capability of the foregoing features, we present the following definitions and conversions.

- (1)  $M_{GD}$ : ground distance of the double-hump in the reconstructed image. Its mathematical expression is shown as follows:

$$M_{GD} = \|P_1 - P_2\|_2 = \sqrt{(x_1 - x_2)^2 + (y_1 - y_2)^2} \approx 2r \quad (7)$$

where  $P_1(x_1, y_1)$  and  $P_2(x_2, y_2)$  respectively represent the coordinates of  $A$  and  $B$  in Fig. 8. In terms of (7),  $M_{GD}$  only depends on landmine's dimension and approximately equals  $2r$ . It seems unsuitable that Eq. (7) is directly used to discriminate

landmine. As a result, we change the judging condition into the following format:

$$3r/2 \leq M_{GD} \leq 5r/2 \tag{8}$$

If the  $M_{GD}$  of the suspected target satisfies Eq. (8), then it will be judged as a landmine; otherwise a clutter.

- (2)  $\varphi$ : azimuth visual angle in the reconstructed image The mathematical expressions of  $A$  and  $B$  are shown as follows:

$$\varphi_A = \tan^{-1}[(x_1 - x_0)/(y_1 - y_0)] \approx \tan^{-1}[(x_2 - x_0)/(y_2 - y_0)] = \varphi_B \tag{9}$$

where  $P_0(x_0, y_0)$  is the ground projection of the virtual aperture center. Thanks to the invariable azimuth scattering property,  $\varphi_A$  should approximately be equivalent to  $\varphi_B$ . However, for the same consideration with  $M_{GD}$ , we select the difference value  $|\Delta\varphi_{AB}|$  as the discriminator. In respect to applicability, Eq. (10) seems more appropriate than Eq. (9).

$$0 \leq |\Delta\varphi_{AB}| < \tan^{-1} \left( \frac{\max \{RRes, ARes\}}{\min \{\|P_1 - P_0\|_2, \|P_2 - P_0\|_2\}} \right) \tag{10}$$

where  $RRes$  and  $ARes$  represent range resolution and cross resolution of the CS reconstructed image, respectively. If the  $|\Delta\varphi_{AB}|$  of the suspected target satisfies Eq. (10), it will be judged as a landmine; otherwise a clutter.

Figure 9 shows the processing flow of the approach, and the primary operation steps are given as follows:

- Original echo pre-processing: system compensation and coupling suppressing;
- CS pre-processing: image region meshing and dictionary construction;

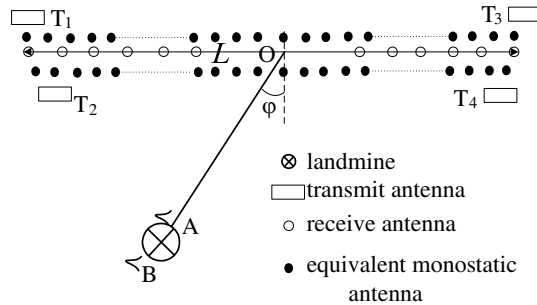


**Figure 8.** Imaging model of the FLGPVAR system.

- MM-IPD processing;
- Feature extraction via Eq. (7) and Eq. (9);
- Landmine discrimination via Eq. (8) and Eq. (10).

## 5. EXPERIMENTAL ANALYSIS

In this section, all the real data are derived from the field experiments of the FLGPVAR system in north China in September 2009. By transmitting the SFCW signal, the FLGPVAR system achieves an ultra wide bandwidth signal, which is from 500 MHz to 2500 MHz with the frequency interval 2 MHz. The height of the linear antenna array is 3.2 m. 16 receive antennae are positioned in the linear array with interval 0.2 m, and 2 transmit antennae are placed at the ends of the array. The test landmine is flush buried with 0.03 m thick soil whose moisture is about 5% to 7%, and its diameter equals 0.3 m. Fig. 10 shows the processing results of one single frame data selected from an actual experiment of the FLGPVAR system. Except for special declaration, all the images are unnormalized amplitude images in ‘dB’ scale within a limit from  $-40$  dB to 0 dB, and the landmine is enclosed with a yellow dash circle. Fig. 10(a) is the image processed by the Back Projection (BP) algorithm with the data of all receive channels and whole frequency band. Based on the statistic of Fig. 10(a), the SNR of landmine is about  $-13.4$  dB. Though the double-hump feature is relatively evident, the low Signal-to-Clutter Ratio (SCR) goes against extracting the consistent features. When using the partial data (40% of the complete data) which is randomly extracted from the complete dataset, this situation will become much worse. As shown in Fig. 10(b), the landmine submerges in the background noise, which means that it has few possibilities to be detected. Fig. 10(c) is the result processed by one single CS reconstruction with the same partial data. By comparison, CS behaves less sensitive to the data missing than BP. As the noise reduces the sparsity of the target in the imaging space, some clutters arise in the CS reconstruction, more or less. After processing the same partial data with the MM-IPD, not only the

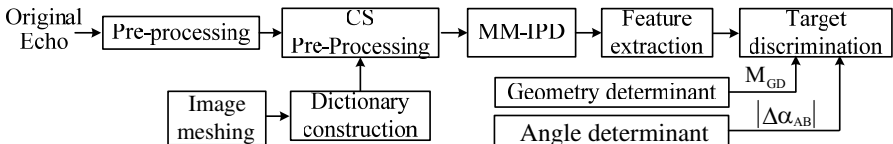


**Figure 9.** The processing flow of the proposed approach.

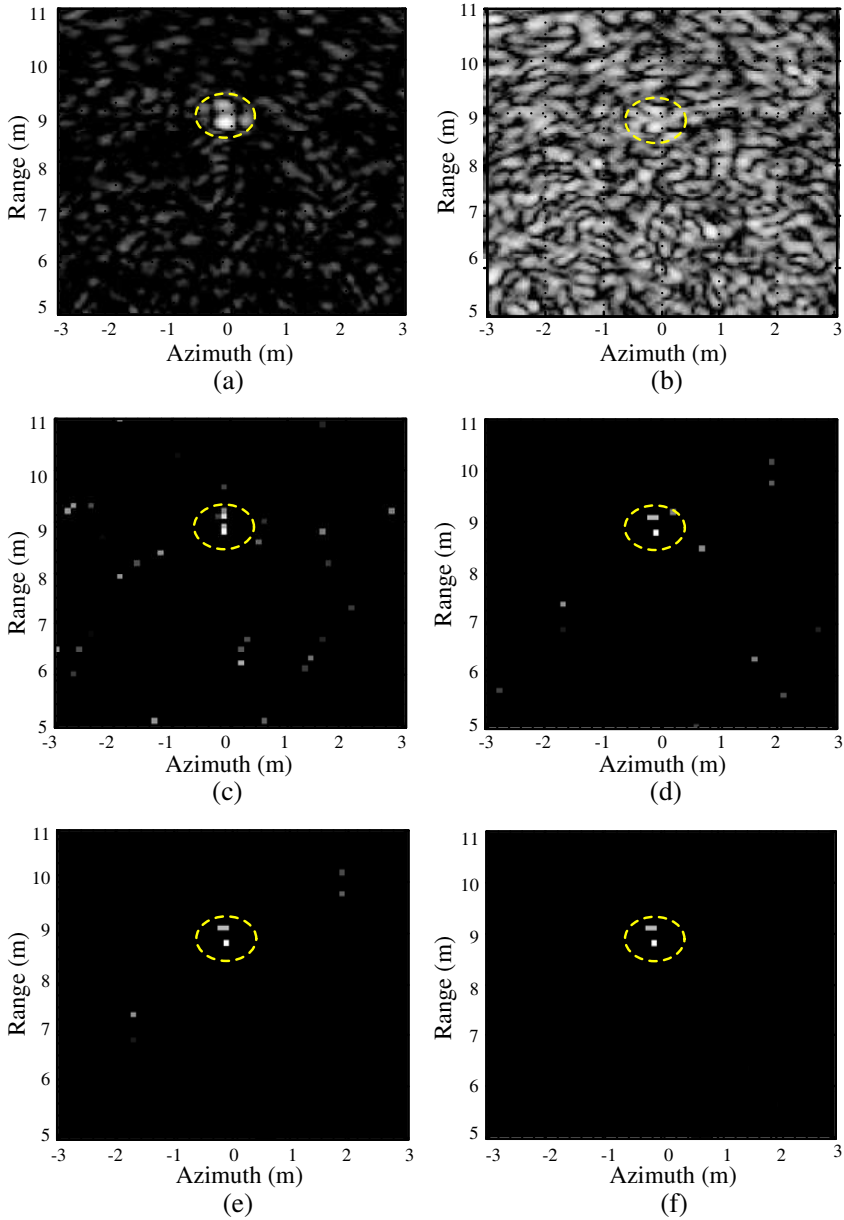


**Figure 10.** (a) BP image with the complete data, (b) BP image with the partial data, (c) CS image with the same partial data, (d) image processed by MM-IPD, (e) and (f) discrimination result with Eq. (8) and Eq. (10).

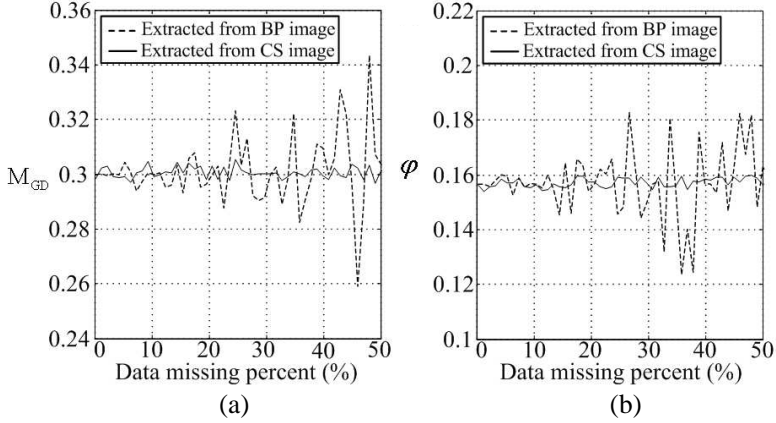


**Figure 11.** Feature curves versus data missing percent: (a)  $M_{GD}$ , (b)  $\alpha$ .

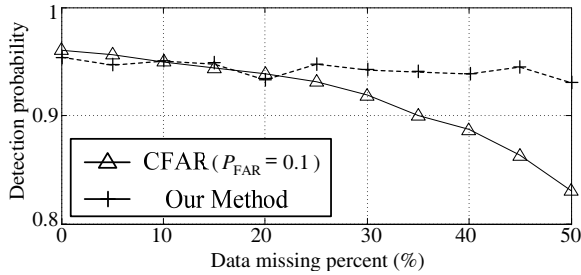


**Figure 12.** ROC curves versus data missing percent.

clutters receive sufficient suppression but also the reconstruction of landmine is enhanced (shown in Fig. 10(d)). Fig. 10(e) and Fig. 10(f) are the discrimination results by virtue of the features in Eq. (8) and Eq. (10), respectively.

To further demonstrate the robustness of the MM-IPD on feature extracting, we present the curves of feature values versus data missing percent in Fig. 11. The results of both  $M_{GD}$  and  $\varphi$  draw the same conclusion that when the data missing percent increases, the features extracted from the BP image deteriorates much heavier than that from the CS image processed by the MM-IPD.

Figure 12 shows the Receive Operating Characteristic (ROC) curves. The false alarm rate  $P_{FAR}$  of the Constant False Alarm Rate (CFAR) detector is set as 0.1. As it was expected, the proposed approach performs better than the CFAR detector, especially when data missing percent is high.

## 6. DISCUSSION AND CONCLUSIONS

A new landmine discrimination approach, which is based on the sparse ESS and apriori knowledge, has been proposed in this paper. This new approach integrates the landmine's ESS with its geometrical feature via CS and extracts the consistent features for discrimination. First, the ESS of landmine is robustly reconstructed with the MM-IPD method. Second, the consistent geometrical parameters of landmine's ESS are extracted from the sparse image. Third, the landmine is effectively discriminated by the geometrical features and apriori knowledge. In the end, the experimental results demonstrate that the propose approach is effective. In this paper, the approach has achieved the integration between imaging and detection by using CS, but it is no more than a novel attempt of applying CS to discriminate the target with sparse ESS in the given environment. Either precondition or foundation of this application demonstrates that there is no horizontal comparison between the conventional methods and ours.

## ACKNOWLEDGMENT

This work was supported by the National Natural Science Foundation of China under Grant 60972121 and 61271441, the Foundation for the Author of National Excellent Doctoral Dissertation of China under Grant 201046, the Program for New Century Excellent Talents in University under Grant NCET-10-0895 and the research project of NUDT under Grand CJ12-04-02.

## REFERENCES

1. Donoho, D. L., "Compressed sensing," *IEEE Transactions on Information Theory*, Vol. 52, No. 4, 1289–1306, 2006.
2. You, Y., H. Xu, C.-S. Li, and L. Zhang, "Data acquisition and processing of parallel frequency SAR based on compressive sensing," *Progress In Electromagnetics Research*, Vol. 133, 199–215, 2013.
3. Li, J., S. Zhang, and J. Chang, "Applications of compressed sensing for multiple transmitters multiple azimuth beams SAR imaging," *Progress In Electromagnetics Research*, Vol. 127, 259–275, 2012.
4. Gurbuz, A. C., H. M. James, and R. S Waymond, "A compressive sensing data acquisition and imaging method for stepped frequency GPRs," *IEEE Transactions on Signal Processing*, Vol. 57, No. 7, 2640–2650, 2009.

5. Wei, S.-J., X.-L. Zhang, J. Shi, and G. Xiang, "Sparse reconstruction for SAR imaging based on compressed sensing," *Progress In Electromagnetics Research*, Vol. 109, 63–81, 2010.
6. Potter, L. C., E. Ertin, J. T. Parker, and M. Cetin, "Sparsity and compressed sensing in radar imaging," *Proceedings of the IEEE*, Vol. 98, No. 6, 1006–1020, Jun. 2010.
7. Wei, S.-J., X.-L. Zhang, and J. Shi, "Linear array SAR imaging via compressed sensing," *Progress In Electromagnetics Research*, Vol. 117, 299–319, 2011.
8. Chen, J., J. Gao, Y. Zhu, W. Yang, and P. Wang, "A novel image formation algorithm for high-resolution wide-swath spaceborne SAR using compressed sensing on azimuth displacement phase center antenna," *Progress In Electromagnetics Research*, Vol. 125, 527–543, 2012.
9. Jin, T. and Z.-M. Zhou, "Imaging model of forward-looking ground penetrating radar with split-aperture transmitting configuration," *2nd Asian and Pacific Conference on Synthetic Aperture Radar*, 21–24, Xi'an, China, 2009.
10. Gonzalez-Huici, M. A. and U. Uschkerat, "GPR modeling for landmine detection," *URSI International Symposium on Electromagnetic Theory*, 152–155, Aug. 2010.
11. Jin, T., J. Lou, and Z. Zhou, "Extraction of landmine features using a forward-looking ground penetrating radar with MIMO array," *IEEE Transactions on Geoscience and Remote Sensing*, Vol. 50, No. 10, 4135–4144, Oct. 2012.
12. Figueiredo, M. A. T., R. D. Nowak, and S. J. Wright, "Gradient Projection for sparse reconstruction: Application to compressed sensing and other inverse problems," *Journal of Selected Topics in Signal Processing: Special Issue on Convex Optimization Methods for Signal Processing*, Vol. 1, No. 4, 586–598, 2007.
13. Batu, O. and M. Cetin, "Parameter selection in sparsity-driven SAR imaging," *IEEE Transactions on Aerospace and Electronic Systems*, Vol. 47, No. 4, 3040–3050, Oct. 2011.
14. Baraniuk, R., "A lecture on compressive sensing," *IEEE Signal Processing Magazine*, Vol. 24, No. 4, 118–121, 2007.
15. Donoho, D. L. and Y. Tsaig, "Extensions of compressed sensing," *Signal Processing*, Vol. 86, No. 3, 533–548, 2006.
16. Potter, L. C., E. Ertin, J. T. Parker, and M. Cetin, "Sparsity and compressed sensing in radar imaging," *Proceedings of the IEEE*, Vol. 98, No. 6, 1006–1020, Jun. 2010.
17. Keogh, E., J. Lin, and W. Truppel, "Clustering of time series

- subsequences is meaningless: Implications for previous and future research,” *Proceedings of the IEEE International Conference on Data Mining*, 115–122, Melbourne, FL, 2003.
18. Anitori, L. and P. Hoogeboom, “False alarm probability estimation for compressive sensing radar,” *IEEE Radar Conference*, 206–211, Kansas City, MO, USA, May 2011.
  19. Wei, H.-Y. and M. Soleimani, “Four dimensional reconstruction using magnetic induction tomography: Experimental study,” *Progress In Electromagnetics Research*, Vol. 129, 17–32, 2012.
  20. Happ, L., F. Le, M. Ressler, and K. Kappra, “Low-frequency ultrawideband synthetic aperture radar: Frequency subbanding for targets obscured by the ground,” *Proceedings of SPIE*, Vol. 2747, 194–201, 1996.
  21. Kositsky, J., “Results from a forward-looking GPR mine detection system,” *Proceedings of SPIE*, Vol. 4038(II), 1077–1087, 2000.
  22. Zeng, T., M. Cherniakov, and T. Long, “Generalized approach to resolution analysis in BSAR,” *IEEE Transactions on Aerospace and Electronic Systems*, Vol. 41, No. 2, 461–474, Apr. 2005.